A Radio Interferometric Couplings Modeling and Analysis Method for 21 cm Cosmology

Shifan Zuo,[1,4] Xuelei Chen,[1,2,3,4]★ Others,
[1]National Astronomical Observatories, Chinese Academy of Sciences, Beijing 100101, China
[2]School of Astronomy and Space Science, University of Chinese Academy of Sciences, Beijing 100049, China
[3]Center of High Energy Physics, Peking University, Beijing 100871, China
[4]Key Laboratory of Radio Astronomy and Technology, Chinese Academy of Sciences, A20 Datun Road, Chaoyang District, Beijing, 100101, P. R. China

Accepted XXX. Received YYY; in original form ZZZ

ABSTRACT

Signal chain reflections and cross coupling between feeds are significant issues for 21 cm cosmological surveys that use modern radio interferometer arrays. These systematics have critical implications for radio surveys that aim to characterize the 21 cm signal from Cosmic Dawn, the Epoch of Reionization (EoR), and the post-EoR period. In this paper, we present a unified matrix-form mathematical modeling and analysis method for signal chain reflections and cross coupling, which we collectively refer to as coupling for simplicity. We then propose a way to solve for the coupling matrix and demonstrate how to correct for couplings by using the solved coupling matrix to mitigate their effects. We also show how couplings are present in the observational data from the Tianlai cylinder array and demonstrate the effectiveness of our method when applied to the observational data.

Key words: radio continuum: 21 cm emission, methods: data analysis

1 INTRODUCTION

The detection and characterization of the 21 cm signal from Cosmic Dawn, the Epoch of Reionization (EoR), and the post-EoR period represent critical milestones in our understanding of the Universe's history. This signal provides a unique window into the process of cosmic structure formation, shedding light on the complex interplay between dark matter, baryons, and radiation (Furlanetto et al. 2006; Morales & Wyithe 2010; Pritchard & Loeb 2012; Zaroubi 2013). As radio surveys delve deeply into these early epochs, the need for high sensitivity and accurate calibration becomes crucial in order to extract meaningful insights (Ansari et al. 2008; Seo et al. 2010; Ansari et al. 2012; Chang et al. 2010; Masui et al. 2013).

Modern radio interferometer arrays are key instruments for 21 cm cosmological surveys due to their ability to achieve high sensitivity and survey large volumes of the sky. A number of completed and ongoing radio interferometric array experiments are targeting the 21 cm intensity mapping and/or its power spectrum measurement, including the Precision Array for Probing the Epoch of Reionization (PAPER; Parsons et al. 2010), the Giant Meterwave Radio Telescope (GMRT; Paciga et al. 2013; Intema et al. 2017), the Murchison Widefield Array (MWA; Bowman et al. 2013), the LOw Frequency Array (LOFAR; Patil et al. 2017; Gehlot et al. 2019), the Hydrogen Epoch of Reionization Array (HERA; DeBoer et al. 2017), the Owens Valley Long Wavelength Array (OVRO-LWA; Eastwood et al. 2018, 2019), the Canadian Hydrogen Intensity Mapping Experiment (CHIME; Newburgh et al. 2014; Amiri et al. 2023), the Hydrogen Intensity and Real-time Analysis eXperiment (HIRAX; Crichton et al. 2022), the Tianlai experiment (Chen 2012; Xu et al. 2015; Li et al. 2020; Wu et al. 2021). Next generation experiments with higher sensitivities are also under construction, including the Canadian Hydrogen Observatory and Radio-transient Detector (CHORD; Vanderlinde et al. 2019), and the Square Kilometre Array (SKA; Koopmans et al. 2015; Maartens et al. 2015). However, these arrays are not without their challenges, as they can be affected by signal chain reflections and cross coupling between feeds, which we will refer to as couplings for simplicity. These systematics can significantly impede the accurate characterization of the 21 cm signal and limit our ability to probe the early Universe (Kern et al. 2019; Li et al. 2021).

Signal chain reflections and cross coupling between feeds are commonly present systematics for 21 cm cosmological surveys using radio interferometer array. Signal chain reflections are generated by impedance mismatches between transmitting surfaces in the analog signal chain when the signal is carried as a voltage. Their effect is to generate a copy of the signal with a time delay and amplitude decay which is superimposed on the original signal. Cross coupling, on the other hand, can occur from a variety of mechanisms, but common sources for radio surveys are stray capacitance between parallel wires or circuit lines in the signal chain (i.e. capacitive crosstalk) and reflections between antennas in the field (i.e. mutual coupling). Cross coupling produces a spurious phase-stable term in the data across time that can occupy a wide range of k modes depending on its origin. They have critical implications for low-frequency radio surveys aiming to characterize the 21 cm signal from the Cosmic Dawn, Epoch of Reionization and the post-EoR period, as these systematics can cause bright foreground emission to contaminate the EoR window and prohibit a robust detection. Kern et al. (2019) has outlined a mathematics for how these systematics appear in interferometric visibilities and described their phenomenology. They then described techniques for modeling and removing these system-

★ E-mail: xuelei@cosmology.bao.ac.cn

atics without attenuating the 21 cm signal in the data. They have used a simpler, algebraic form for the visibility equation with an assumption of a three-parameter form of the coupling coefficient $\epsilon_{ij}(\nu) = A_{ij}e^{2\pi i\tau_{ij}\nu+i\phi_{ij}}$ with parameters A_{ij}, τ_{ij} and ϕ_{ij}, where when $i = j$ it is the coupling coefficient describing the signal chain reflection of feed i, while when $i \neq j$, it is the coupling coefficient describing the cross coupling between feed i and j. The fit of the parameters and then removal of the systematics are done in delay domain, i.e. the Fourier conjugate of the frequency domain. In a companion paper, they have applied these techniques to data from HERA's first observing season as a method demonstration (Kern et al. 2020). Li et al. (2021) have also used a similar method to model and remove reflections and standing waves on the Tianlai cylinder array.

In this paper, we present a different mathematical framework to model and analyze couplings in radio interferometer arrays. Unlike the simpler, algebraic form visibility equation form of Kern et al. (2019), we introduce a unified matrix-form representation of signal chain reflections and cross coupling, providing a systematic approach to understand and mitigate their effects. Also we do not assume a specific parametric form for the coupling coefficients and not work in the delay domain. Our proposed method offers a path to solve for the coupling matrix, which can then be used to correct for couplings in the observational data.

To demonstrate the effectiveness of our method, we apply it to real-world observational data from the Tianlai cylinder array, a cutting-edge radio interferometer array designed for 21 cm cosmological surveys. We have shown how the couplings are present in the Tianlai cylinder array's data, and how our proposed method can successfully mitigate their effects, paving the way for more accurate detections and characterizations of the 21 cm signal.

This work is organized as follows:

2 METHOD

We describe how signal chain reflections and cross coupling between feeds appear in interferometric data products.

To begin, we start with a two-element interferometer (Thompson et al. 1986; Taylor et al. 1999; Hamaker et al. 1996; Smirnov 2011), consisting of two antennas, i and j, whose feeds measure an incident electric field and convert it into a voltage. In Figure 1, we show a schematic of the two-element system and mark possible sources of signal chain reflections and cross coupling between feeds. These signals travel from the feeds through each antenna's signal chain to the a correlator, and along the way are amplified, digitized, channelized, and Fourier transformed into the frequency domain. The correlator then cross multiplies voltage spectra to form the fundamental interferometric data product: the cross correlation visibility, V_{ij}, between feed i and j, written as

$$V_{ij} = \langle v_i v_j^* \rangle. \tag{1}$$

2.1 Signal Chain Reflections

If v_i is antenna i's voltage without a signal chain reflection, then the presence of a reflection can be encapsulated as

$$v_i' = v_i + \epsilon_{ii} v_i, \tag{2}$$

where ϵ_{ii} is the coupling coefficient describing the signal chain reflection of feed i.

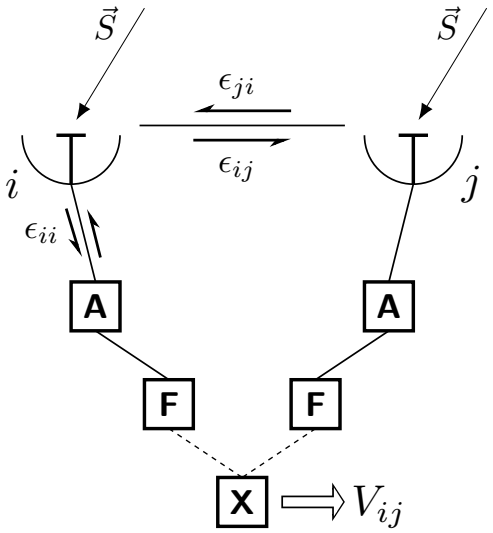

Figure 1. The signal chain reflections and cross coupling model. The signal from the sky, denoted by $\vec{S}$, enters the feed of each antenna and is transformed into a voltage, which then travels down the signal chain. At a certain point, the signal is amplified by an amplifier (**A**). Next, the signal is sent to an engine that digitizes and Fourier transforms it (**F**), and then to the correlator (**X**), which produces the visibility V_{ij}. Any possible cable reflection in the signal chain of feed i is indicated by ϵ_{ii}, which travels up and down the cable that connects the feed to the node. Possible cross-coupling is marked as ϵ_{ij}, which occurs when radiation is reflected off of feed j and into feed i, or vice versa. The dashed lines indicate the signal pathway after digitization, where internal instrument coupling is no longer a major concern.

2.2 Antenna Cross Coupling

We describe the cross coupling between feeds i and j as

$$v_i' = v_i + \sum_j \epsilon_{ij} v_j, \tag{3}$$

for all $j \neq i$, where ϵ_{ij} is the coupling coefficient.

Note the summation in Equation 3, unlike in Kern et al. (2019) where the authors only consider coupling between two feeds, here we take into account cross coupling between a specific feed and all other feeds of the array.

2.3 Unified Modeling

We give unified modeling of signal chain reflections and cross coupling between feeds as

$$v_i' = v_i + \sum_j \epsilon_{ij} v_j, \tag{4}$$

where when $i = j$, it describes reflections in feed i's signal chain, and when $i \neq j$, it describes cross coupling between feeds i and j. Writing in vector form, this is

$$\boldsymbol{v}' = \boldsymbol{v} + \boldsymbol{\Xi}\boldsymbol{v} = (\boldsymbol{I} + \boldsymbol{\Xi})\boldsymbol{v}, \tag{5}$$

where $\boldsymbol{\Xi}$ is a matrix with elements of all the coupling coefficients ϵ_{ij}, we call it as the coupling matrix for simplicity.

The visibility matrix would be

$$\boldsymbol{V}' = \langle \boldsymbol{v}'\boldsymbol{v}'^{\dagger} \rangle = (\boldsymbol{I} + \boldsymbol{\Xi})\langle \boldsymbol{v}\boldsymbol{v}^{\dagger} \rangle (\boldsymbol{I} + \boldsymbol{\Xi}^{\dagger}) = (\boldsymbol{I} + \boldsymbol{\Xi})\boldsymbol{V}(\boldsymbol{I} + \boldsymbol{\Xi}^{\dagger}). \tag{6}$$

For simplicity, in the following, we will unitedly refer to the signal chain reflections and cross coupling between feeds as couplings.

2.4 With Gain Calibration

In practice, the observed visibilities need to be calibrated for an unknown gain. Here, we assume that the unknown gains are feed based, i.e. the un-calibrated visibilities can be described as $V_{ij}^{\rm uncal} = g_i g_j^* V_{ij}^{\rm true}$ for all feed pairs (i, j). Using the vector-matrix form description of the couplings, we have the observed un-calibrated visibility as

$$\boldsymbol{V}' = (\boldsymbol{I} + \boldsymbol{\Xi})\boldsymbol{G}\boldsymbol{V}\boldsymbol{G}^\dagger(\boldsymbol{I} + \boldsymbol{\Xi}^\dagger). \tag{7}$$

where $\boldsymbol{G}$ is a diagonal matrix whose i-th diagonal element is the gain g_i of the i-th feed. The gain $\boldsymbol{G}$ could be solved by, e.g. eigenvector-based point source calibration method (Zuo et al. 2019), and we demonstrate in Appendix A that the coupling has only a minor effect on the eigenvector-based calibration method. If $\boldsymbol{G}$ is known, we can have

$$\boldsymbol{G}^{-1}\boldsymbol{V}'\boldsymbol{G}^{-\dagger} = \boldsymbol{G}^{-1}(\boldsymbol{I} + \boldsymbol{\Xi})\boldsymbol{G}\boldsymbol{V}\boldsymbol{G}^\dagger(\boldsymbol{I} + \boldsymbol{\Xi}^\dagger)\boldsymbol{G}^{-\dagger} \tag{8}$$

$$= (\boldsymbol{I} + \boldsymbol{G}^{-1}\boldsymbol{\Xi}\boldsymbol{G})\boldsymbol{V}(\boldsymbol{I} + (\boldsymbol{G}^{-1}\boldsymbol{\Xi}\boldsymbol{G})^\dagger). \tag{9}$$

Now if we re-write the gain calibrated visibility matrix $\boldsymbol{G}^{-1}\boldsymbol{V}'\boldsymbol{G}^{-\dagger}$ as $\boldsymbol{V}'$, and re-write $\boldsymbol{G}^{-1}\boldsymbol{\Xi}\boldsymbol{G}$ as $\boldsymbol{\Xi}$, we again get

$$\boldsymbol{V}' = (\boldsymbol{I} + \boldsymbol{\Xi})\boldsymbol{V}(\boldsymbol{I} + \boldsymbol{\Xi}^\dagger), \tag{10}$$

which has the same form as Equation 6.

Appendix A has a detailed discussion on the impact of coupling on the eigenvector-based calibration method, and it also shows that the combination of the eigenvector-based calibration method and the coupling modeling and correction method discussed in this paper would accurately calibrate the array and mitigate the effects of the coupling.

2.5 Solve Coupling Matrix

The eigenvalue decomposition of $\boldsymbol{V}'$ and $\boldsymbol{V}$ are

$$\boldsymbol{V}' = \boldsymbol{U}'\boldsymbol{\Lambda}'\boldsymbol{U}'^\dagger, \tag{11}$$

$$\boldsymbol{V} = \boldsymbol{U}\boldsymbol{\Lambda}\boldsymbol{U}^\dagger, \tag{12}$$

where $\boldsymbol{\Lambda}$ ($\boldsymbol{\Lambda}'$) is a diagonal matrix with its diagonal elements being the eigenvalues of $\boldsymbol{V}$ ($\boldsymbol{V}'$), and $\boldsymbol{U}$ ($\boldsymbol{U}'$) is a unitary matrix with its columns the eigenvectors of $\boldsymbol{V}$ ($\boldsymbol{V}'$). Because of $v_{ji} = v_{ij}^*$, the visibility matrix $\boldsymbol{V}$ (or $\boldsymbol{V}'$) is Hermitian, all eigenvalues are real numbers.

Substitute the eigenvalue decomposition of $\boldsymbol{V}'$ and $\boldsymbol{V}$ into Equation 6 (or Equation 10), we have

$$(\boldsymbol{U}'\boldsymbol{\Lambda}'^{\frac{1}{2}})(\boldsymbol{\Lambda}'^{\frac{1}{2}}\boldsymbol{U}'^\dagger) = [(\boldsymbol{I} + \boldsymbol{\Xi})\boldsymbol{U}\boldsymbol{\Lambda}^{\frac{1}{2}}][\boldsymbol{\Lambda}^{\frac{1}{2}}\boldsymbol{U}^\dagger(\boldsymbol{I} + \boldsymbol{\Xi}^\dagger)], \tag{13}$$

which gives

$$(\boldsymbol{I} + \boldsymbol{\Xi})\boldsymbol{U}\boldsymbol{\Lambda}^{\frac{1}{2}} = \boldsymbol{U}'\boldsymbol{\Lambda}'^{\frac{1}{2}}, \tag{14}$$

from this we can solve the coupling matrix as

$$\boldsymbol{I} + \boldsymbol{\Xi} = (\boldsymbol{U}'\boldsymbol{\Lambda}'^{\frac{1}{2}})(\boldsymbol{U}\boldsymbol{\Lambda}^{\frac{1}{2}})^{-1}. \tag{15}$$

Actually there are some degeneracies in solving for the coupling matrix, we will discuss it in more detail in Section 2.6.

After we have solved the coupling matrix, the coupling-corrected visibility can be obtained as

$$\tilde{\boldsymbol{V}} = (\boldsymbol{I} + \boldsymbol{\Xi})^{-1}\boldsymbol{V}'(\boldsymbol{I} + \boldsymbol{\Xi}^\dagger)^{-1}. \tag{16}$$

In real applications, the exact inverse of the matrices in Equation 15 and Equation 16 may not exist due to singularities, in such cases we will use the Moore–Penrose pseudoinverse instead. This is also true for the following discussions where the inverse of a matrix is involved.

2.6 Degeneracy

There are some degeneracies in solving for the coupling matrix. For an arbitrary unitary matrix $\boldsymbol{K}$, we have $\boldsymbol{K}\boldsymbol{K}^\dagger = \boldsymbol{I}$, so we have

$$(\boldsymbol{U}'\boldsymbol{\Lambda}'^{\frac{1}{2}}\boldsymbol{K})(\boldsymbol{K}^\dagger\boldsymbol{\Lambda}'^{\frac{1}{2}}\boldsymbol{U}'^\dagger) = [(\boldsymbol{I} + \boldsymbol{\Xi})\boldsymbol{U}\boldsymbol{\Lambda}^{\frac{1}{2}}][\boldsymbol{\Lambda}^{\frac{1}{2}}\boldsymbol{U}^\dagger(\boldsymbol{I} + \boldsymbol{\Xi}^\dagger)], \tag{17}$$

from this we get the solved coupling matrix as

$$\boldsymbol{I} + \boldsymbol{\Xi} = (\boldsymbol{U}'\boldsymbol{\Lambda}'^{\frac{1}{2}}\boldsymbol{K})(\boldsymbol{U}\boldsymbol{\Lambda}^{\frac{1}{2}})^{-1}. \tag{18}$$

Due to the indeterminacy of the arbitrary unitary matrix $\boldsymbol{K}$, the coupling matrix $\boldsymbol{\Xi}$ could not be uniquely determined. But we can find that this degeneracy does not affect the coupling correction process Equation 16 as the undetermined arbitrary unitary matrix $\boldsymbol{K}$ is canceled out in the coupling correction process, as can be shown in the following calculation:

$$\tilde{\boldsymbol{V}} = (\boldsymbol{I} + \boldsymbol{\Xi})^{-1}\boldsymbol{V}'(\boldsymbol{I} + \boldsymbol{\Xi}^\dagger)^{-1},$$

$$= (\boldsymbol{U}\boldsymbol{\Lambda}^{\frac{1}{2}})[(\boldsymbol{U}'\boldsymbol{\Lambda}'^{\frac{1}{2}}\boldsymbol{K})^{-1}(\boldsymbol{U}'\boldsymbol{\Lambda}'^{\frac{1}{2}}\boldsymbol{K})(\boldsymbol{K}^\dagger\boldsymbol{\Lambda}'^{\frac{1}{2}}\boldsymbol{U}'^\dagger)(\boldsymbol{K}^\dagger\boldsymbol{\Lambda}'^{\frac{1}{2}}\boldsymbol{U}'^\dagger)^{-1}](\boldsymbol{\Lambda}^{\frac{1}{2}}\boldsymbol{U}^\dagger).$$

In the above calculation, some of the inverse may need to be replaced with an inexact Moore–Penrose pseudoinverse, but the unitary matrix $\boldsymbol{K}$ has an exact inversion, so it will be canceled out.

3 OBSERVATION AND COUPLINGS EFFECTS

We utilize observational data from the Tianlai cylinder array to examine the couplings and their potential impact on characterizing the 21 cm signal that the array aims to detect.

The Tianlai project, which translates to "heavenly sound" in Chinese, is a 21 cm intensity mapping (IM) experiment (Chen 2012; Xu et al. 2015; Zhang et al. 2016b,a). The pathfinder experiment comprises a cylinder array and a dish array, both situated at the Hongliuxia site (91°48′E,44°09′N) in Xinjiang, northwest China. The experiment's objective is to test the principles and key technologies for conducting large-scale structure surveys of the neutral hydrogen distribution within the redshift range of 0 – 3.

The Tianlai cylinder pathfinder is a radio interferometer array designed to test techniques for 21 cm intensity mapping in the post-reionization Universe. Its ultimate goal is to map the large-scale structure and measure cosmological parameters, such as the dark energy equation of state. The array consists of three parallel cylinder reflectors oriented in the north-south direction, providing a large field of view. As the Earth rotates, the northern sky is observed through drift scanning. Each of the three parallel cylindrical reflectors has a width of 15 meters and a length of 40 meters. From east to west, 31, 32, and 33 feeds are evenly installed on the three cylinders, respectively. The distance between the northernmost and southernmost feeds is 12.4 meters. Figure 2 presents a schematic diagram of the three cylinders and the configuration of the feeds. Since its first light observation in early 2016, the Tianlai cylinder pathfinder array has collected a substantial amount of data (Das et al. 2018; Li et al. 2020; Wu et al. 2021). The data used in this analysis is a single day's observational data recorded on September 27, 2016.

Figure 3 gives a schematic data processing flow for the coupling modeling and analysis results give in this paper. We have used the

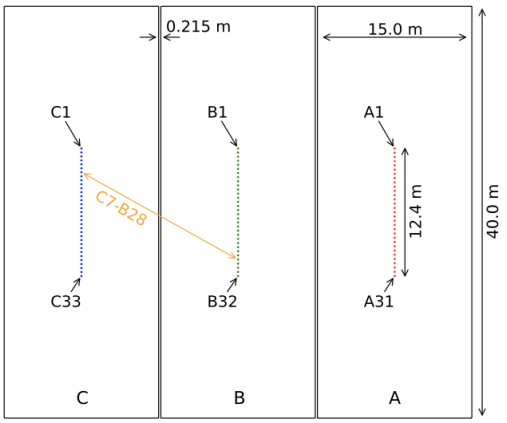

Figure 2. The Tianlai Cylinder Array. The cylinders are aligned in the N-S direction, with a gap of 0.215 m between adjacent ones. The three cylinders are designated as A, B, C from east to west, and have 31, 32, and 33 feeds respectively. The feeds in each cylinder are evenly distributed, with the ones at both ends (A1, B1, C1 in the north and A31, B32, C33 in the south) aligned with each other.

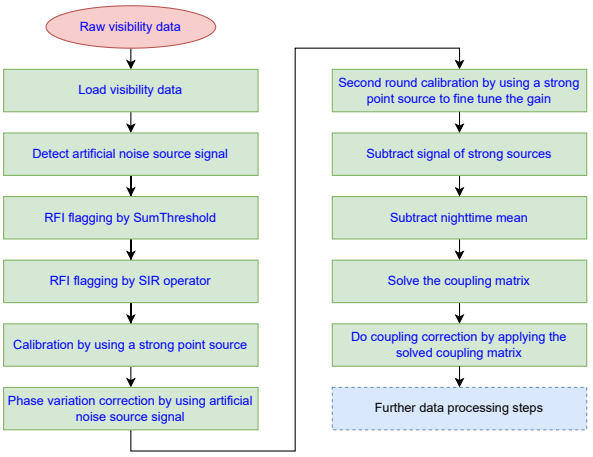

Figure 3. Data processing and analysis pipeline for coupling correction. The last square with dash line boundary is some further data processing steps that are not discussed in this paper, See Zuo et al. 2023, in preparation for detail.

Tialai data process pipeline `tlpipe`[1] (Zuo et al. 2021) for the data processing and analysis work. After loading the observational data from the raw visibility data files on disk, we first detect the signal of the artificial noise source, which was periodically broadcasted to correct relative phase variations over time. Next, we detect and set corresponding masks for strong radio frequency interferences (RFIs) present in the data using the SumThreshold (Offringa et al. 2010) and the SIR operator method (Offringa et al. 2012). We then employ an eigenvector-based method to extract the signal of a strong point source (Cygnus A) and use the extracted signal to calibrate the observational data (Zuo et al. 2019). The relative phase change over time is calibrated using the artificial noise source signal. Following this, we fine-tune the gain of the array using the extracted signal of the calibrator Cygnus A with the same eigenvector-based calibration method. This completes our calibration process, and we proceed to subtract the extracted signal of strong sources from the data. We then subtract the nighttime mean from the calibrated and strong sources subtracted data, and from that, we will solve a coupling matrix and perform coupling correction by applying the solved coupling matrix. The nighttime mean subtraction and coupling correction process will be detailed in Section 4.

3.1 The Non-flat Bandpass

We noticed that the bandpass of the Tianlai cylinder observational data is non-flat, particularly for short baselines composed of two feeds located on the same cylinder, even after the calibration process. In Figure 4, we display the observed visibilities before and after calibration for four baselines: $(10, 11)$, $(10, 20)$, $(10, 40)$, and $(10, 80)$ at a time point around midnight when no strong sources are in transit. Baseline $(10, 11)$ consists of two adjacent feeds on the same cylinder, baseline $(10, 20)$ consists of two non-adjacent feeds on the same cylinder, baseline $(10, 40)$ consists of two feeds on two adjacent cylinders, and baseline $(10, 80)$ consists of two feeds on two non-adjacent cylinders. We find that the bandpass of baselines comprising feeds on the same cylinder, even when the feeds are not adjacent, varies significantly. Calibration does not effectively flatten the bandpass as one might expect. The bandpass of baselines consisting of feeds on different cylinders is much flatter, particularly for feeds on non-adjacent cylinders.

To examine the effects of calibration on the bandpass, we also plotted the observed visibilities and the extracted Cygnus A signal before and after calibration for the same four baselines: $(10, 11)$, $(10, 20)$, $(10, 40)$, and $(10, 80)$ at the transit time of the calibrator Cygnus A in Figure 5. Additionally, we plotted the frequency spectrum of Cygnus A (the black line) in Figure 5. The method for extracting a strong point source's signal from the observed visibility data and using it for array calibration is described in Zuo et al. (2019). We observe that the extracted Cygnus A signal is non-flat before calibration, but the calibration process has flattened it to match Cygnus A's frequency spectrum. As shown in Figure 4, the observed visibilities have a highly non-flat bandpass before calibration. However, after calibration, the visibilities observed by baselines consisting of feeds on different cylinders become relatively flattened, approaching Cygnus A's spectrum. This effect is even more pronounced for the longest baselines consisting of feeds on non-adjacent cylinders. This is not the case for the visibilities observed by baselines consisting of feeds on the same cylinder, even when the feeds are not adjacent.

Figure 4 and Figure 5 clearly demonstrate couplings between feeds, particularly for feeds on the same cylinder.

3.2 The Visibility Matrix

For better analyzing couplings between feeds, we plot the visibility matrix in Figure 6, where we have shown the observed visibilities before (top) and after (bottom) calibration at observing frequency 750 MHz at a time point in the middle of the night when there is no strong sources transit. We can obviously see three squares in either the un-calibrated visibility matrix or the calibrated visibility matrix along the main diagonal. Inside each square is the visibility observed by baselines consisting of feeds on the same cylinder. Their significantly higher visibility magnitude is due to higher couplings between the feeds on the same cylinder. The couplings between feeds on different cylinders are much weaker.

We have also shown the observed visibilities, the extracted calibrator's signal and the residual visibilities before (top) and after

[1] https://github.com/TianlaiProject/tlpipe

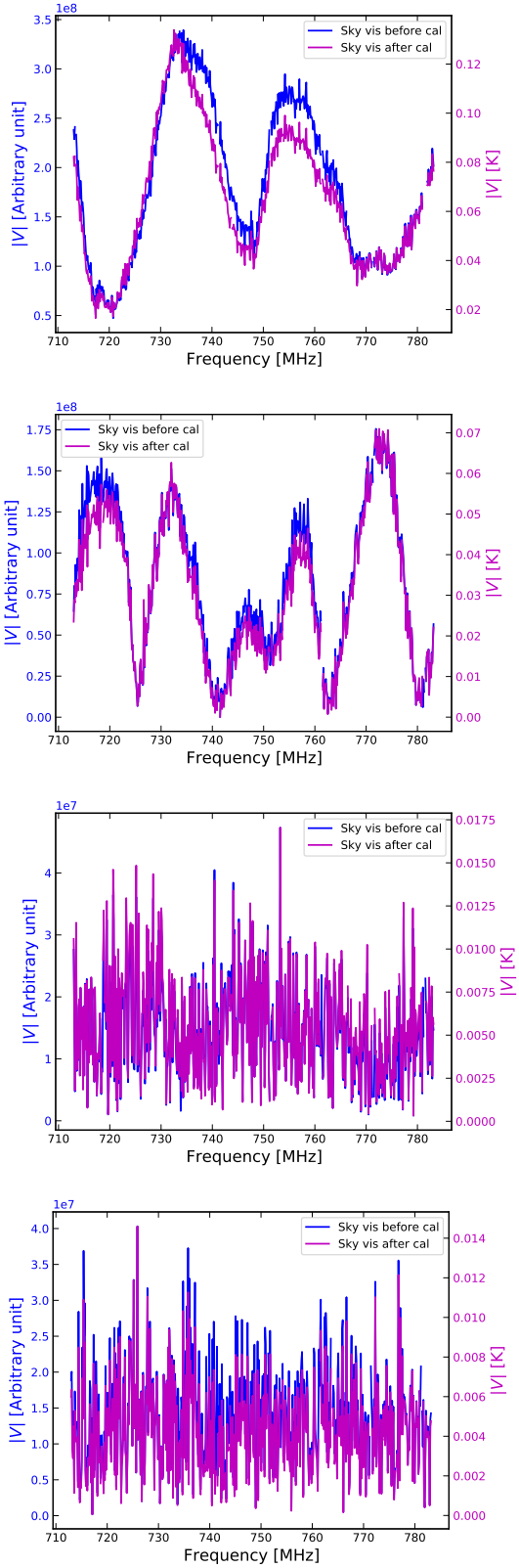

Figure 4. Observed visibilities (only magnitude) before and after calibration for four baselines: $(10, 11)$, $(10, 20)$, $(10, 40)$ and $(10, 80)$ at a time point in the middle of the night when there are no strong sources transit. The value of un-calibrated visibilities have arbitrary unit and the calibrated visibilities have unit brightness temperature K. We have shown the XX polarization visibilities only, the YY polarization visibilities are similar.

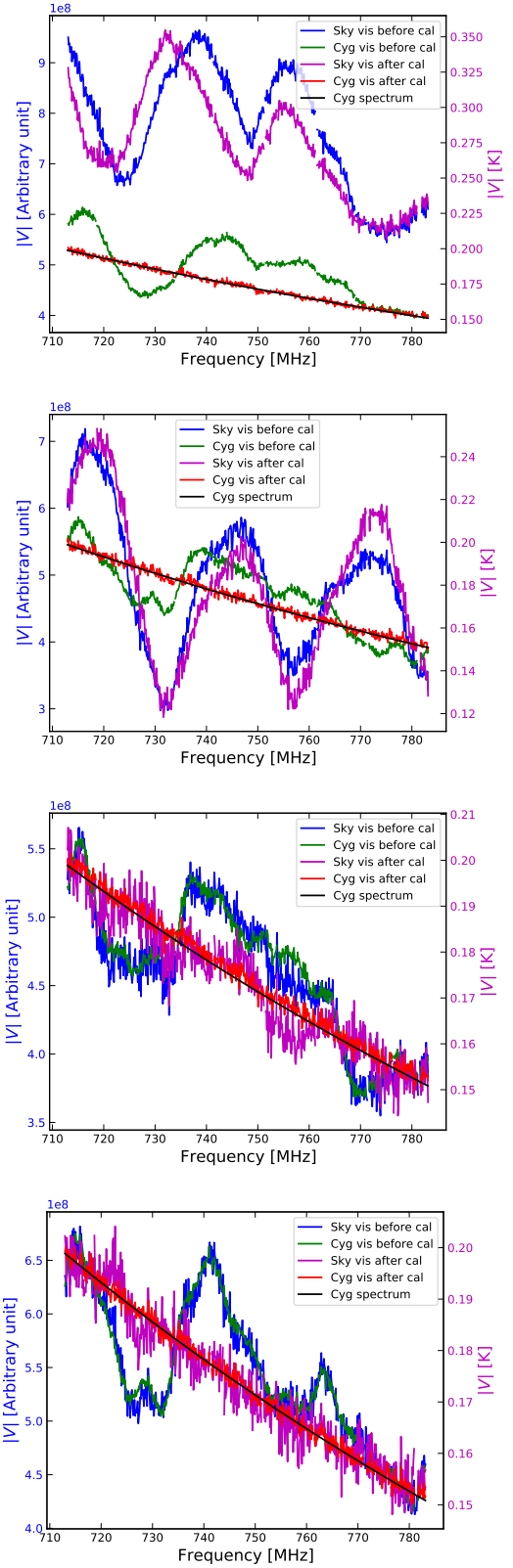

Figure 5. Observed visibilities (only magnitude) before and after calibration for four baselines: $(10, 11)$, $(10, 20)$, $(10, 40)$ and $(10, 80)$ at the transit time of the calibrator Cygnus A. The value of un-calibrated visibilities have arbitrary unit and the calibrated visibilities have unit brightness temperature K. We have shown the XX polarization visibilities only, the YY polarization visibilities are similar.

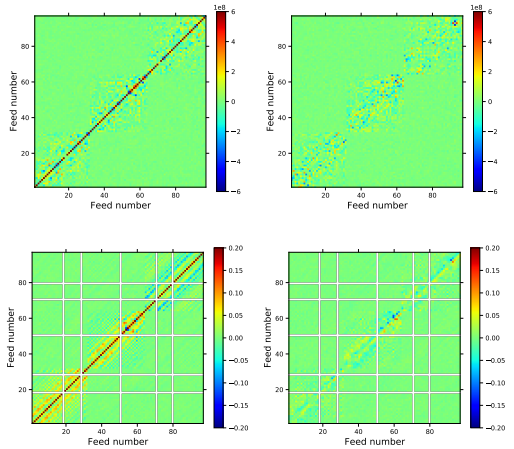

Figure 6. Observed visibilities before (top) and after (bottom) calibration at observing frequency 750 MHz at a time point in the middle of the night when there are no strong sources transit. Left is for real part, right is for imaginary part. The empty horizontal and vertical lines in the bottom are masked visibilities due to malfunctioning feeds. The values of un-calibrated visibilities have arbitrary unit and the calibrated visibilities have unit brightness temperature K. We have shown the XX polarization visibilities only, the YY polarization visibilities are similar.

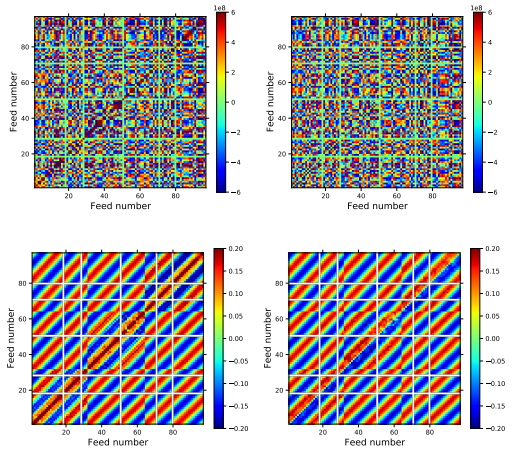

Figure 7. Observed visibilities before (top) and after (bottom) calibration at observing frequency 750 MHz at the transit time of the calibrator Cygnus A. Left is for real part, right is for imaginary part. The empty horizontal and vertical lines in the bottom are masked visibilities due to malfunctioning feeds. The value of un-calibrated visibilities have arbitrary unit and the calibrated visibilities have unit brightness temperature K. We can see clear fringes in the bottom which are the dominant signal of the calibrator. We have shown the XX polarization visibilities only, the YY polarization visibilities are similar.

(bottom) calibration at observing frequency 750 MHz at the transit time of the calibrator Cygnus A in Figure 7, Figure 8 and Figure 9, respectively. This again shows that conventional calibration process does not help to alleviate couplings between feeds.

To accurately characterize the 21 cm signal we are trying to detect, we need to take special care of the couplings in addition to the accurate calibration process. We will show how the couplings are modeled and corrected by using our developed method described in Section 2 in the following Section.

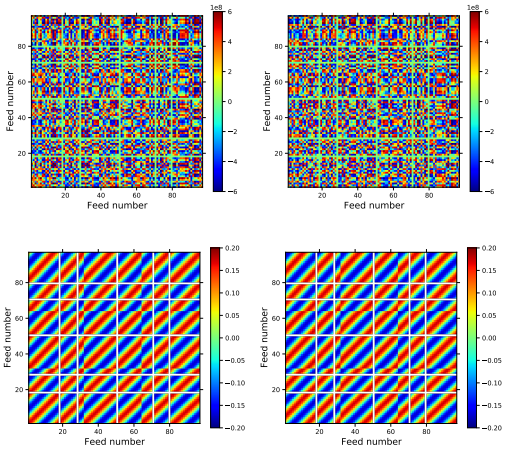

Figure 8. The extracted calibrator's signal before (top) and after (bottom) calibration at observing frequency 750 MHz at the transit time of the calibrator Cygnus A. Left is for real part, right is for imaginary part. The empty horizontal and vertical lines in the bottom are masked visibilities due to malfunctioning feeds. The value of un-calibrated visibilities have arbitrary unit and the calibrated visibilities have unit brightness temperature K. We have shown the XX polarization visibilities only, the YY polarization visibilities are similar.

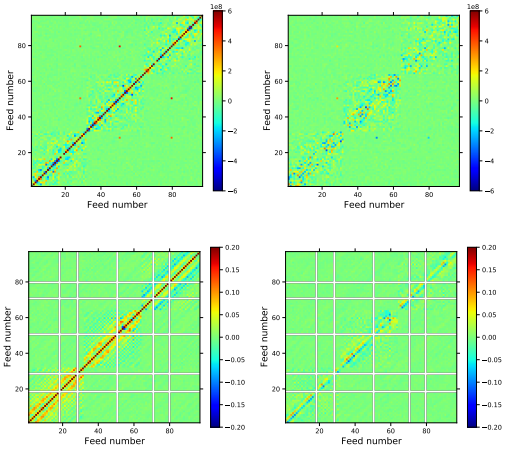

Figure 9. The residual visibilities (i.e. the difference between Figure 7 and Figure 8) before (top) and after (bottom) calibration at observing frequency 750 MHz at the transit time of the calibrator Cygnus A. Left is for real part, right is for imaginary part. The empty horizontal and vertical lines in the bottom are masked visibilities due to malfunctioning feeds. The values of un-calibrated visibilities have arbitrary unit and the calibrated visibilities have unit brightness temperature K. We have shown the XX polarization visibilities only, the YY polarization visibilities are similar.

4 COUPLING CORRECTION

4.1 Nighttime Mean

We anticipate that the couplings will be relatively stable over a certain time period (on the order of hours), particularly around midnight. This stability is confirmed and can be observed in Figure 10, where we present a 2-hour waterfall plot of the calibrated and strong point sources subtracted visibilities around midnight.

Assuming that the couplings between feeds remain stable at least around midnight, we can eliminate the couplings by subtracting the

nighttime mean from the calibrated visibilities with strong point sources subtracted. In practice, the couplings are not entirely static, as they change slowly over time. Consequently, we cannot expect the nighttime mean subtraction process to completely eliminate the couplings. Additionally, any steady component (i.e., the DC component) of the visibility is subtracted out in this process, although the DC component does not affect the final map-making of an interferometer array. Nevertheless, we observe that the nighttime mean subtraction process has eliminated most of the couplings, as demonstrated in Figure 10 and Figure 11. From Figure 11, we also note that different baselines have varying couplings and DC components, resulting in different amounts of nighttime mean being subtracted for redundant baselines. This causes redundant baselines to have significantly different residual visibilities, as seen in the diagonal elements in the bottom panel of Figure 11. In theory, redundant baselines should have the same measurements, so this discrepancy should not occur. We will address this issue in the following subsection. Another notable observation is that, when comparing the left and right panels of Figure 10, some weak RFIs become apparent in the nighttime mean subtracted data. These RFIs will be further flagged in subsequent data processing steps. As this is not directly related to the coupling modeling and removal analysis results presented in this paper, we will not discuss it further.

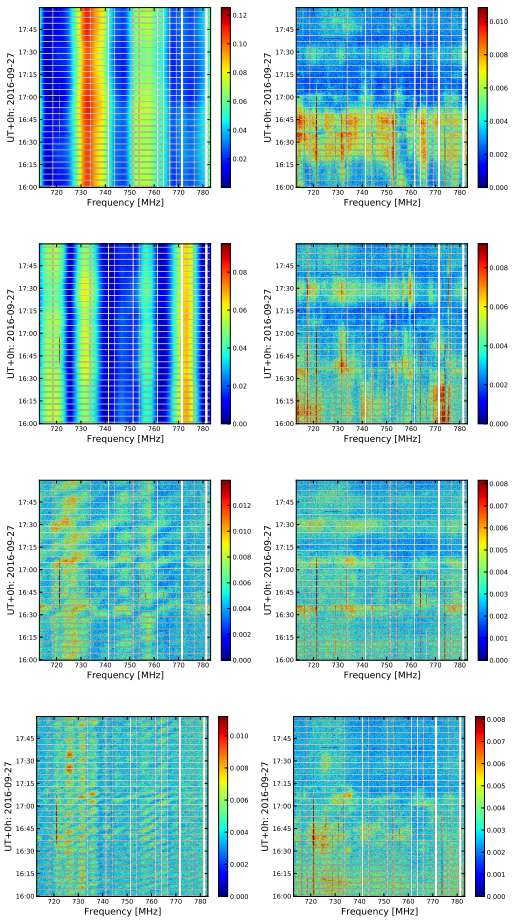

Figure 10. Two hours waterfall plot of the calibrated and strong point sources subtracted visibilities (left) and the nighttime mean subtracted visibilities (right) observed by four baselines: $(10, 11)$, $(10, 20)$, $(10, 40)$ and $(10, 80)$ at midnight (0:00 am —- 02:00 am Beijing time). The empty regularly spaced horizontal lines are masked artificial noise source signal, the empty vertical lines are RFI flagged values. We have plotted only the magnitude of the visibility, and the unit of the visibilities is brightness temperature K. We have shown the XX polarization visibilities only, the YY polarization visibilities are similar.

4.2 Solve Coupling

The nighttime mean subtraction process is unable to fully eliminate the couplings between feeds and may subtract varying amounts of DC components, as observed and discussed in the previous subsection. To further eliminate the couplings between feeds, we can attempt to solve for the coupling matrix and use the resulting matrix for coupling correction.

The method is detailed in Section 2.5. However, to solve the coupling matrix, we need to know the true visibility matrix $\boldsymbol{V}$. This can be obtained in various ways. One approach is to use simulation, generating visibilities by employing the model Tianlai cylinder array and beam to observe a realistic sky model, such as the Global Sky Model (de Oliveira-Costa et al. 2008; Zheng et al. 2017). Currently, due to uncertainties in the Tianlai cylinder beam model and other complexities, the visibilities generated by simulations may significantly differ from the true visibilities. Here, we choose an alternative method. We take the nighttime mean subtracted visibilities as an approximation of the true visibilities that are free from couplings. After performing eigen-decomposition of the calibrated and strong sources subtracted visibility matrix (denoted as $\boldsymbol{V}'$) and the nighttime mean subtracted visibility matrix (denoted as $\boldsymbol{V}$), we can solve the coupling matrix as in Equation 15. We then obtain the coupling corrected visibility matrix $\tilde{\boldsymbol{V}}$ by applying the solved coupling matrix as in Equation 16. The coupling corrected visibility matrix $\tilde{\boldsymbol{V}}$ is shown in the top panel of Figure 12. The issue of redundant baselines having significantly different values still persists, as can be clearly seen in the diagonal elements of the coupling corrected visibility matrix $\tilde{\boldsymbol{V}}$. We address this as follows.

We take all the unmasked diagonal elements of $\tilde{\boldsymbol{V}}$ as a vector $\boldsymbol{v}$. As the diagonal elements are measurements from auto-correlations, they are all real numbers. We compute the mean of all the elements of $\boldsymbol{v}$ as m and the element-wise square root of $\boldsymbol{v}$ as a vector $\boldsymbol{g}$. We obtain the diagonal element normalized visibility matrix $\tilde{\boldsymbol{V}}n = m\tilde{\boldsymbol{V}} \oslash \boldsymbol{g}\boldsymbol{g}^T$, where $\oslash$ represents element-wise division. We then take $\tilde{\boldsymbol{V}}n$ as an updated approximation of the true visibility matrix and perform an eigen-decomposition of $\tilde{\boldsymbol{V}}n$ to solve a new coupling matrix. We use this new coupling matrix to obtain a new coupling corrected visibility matrix $\tilde{\boldsymbol{V}}_1$ by applying the new coupling matrix as in Equation 16. We refer to $\tilde{\boldsymbol{V}}_1$ as the coupling corrected visibility matrix with diagonal correction and display it in the bottom panel of Figure 12. Comparing the top panel with the bottom panel, we observe that the coupling corrected visibility matrix with diagonal correction has more evenly distributed diagonal elements than the coupling corrected visibility matrix without diagonal correction.

Figure 13 displays the strong point sources subtracted visibilities before and after nighttime mean subtraction and coupling correction for four baselines: $(10, 11)$, $(10, 20)$, $(10, 40)$, and $(10, 80)$ at the transit time of the calibrator Cygnus A. We observe that the subtracted nighttime mean can account for most of the couplings for short baselines, and our coupling modeling and correction method can effectively mitigate the remaining couplings. The bandpasses after the coupling correction become much flatter than the original ones for both short and long baselines. However, we also observed that some exceptionally high sticky-like values appeared in the coupling-corrected visibilities, which may be due to unstable inversion of the

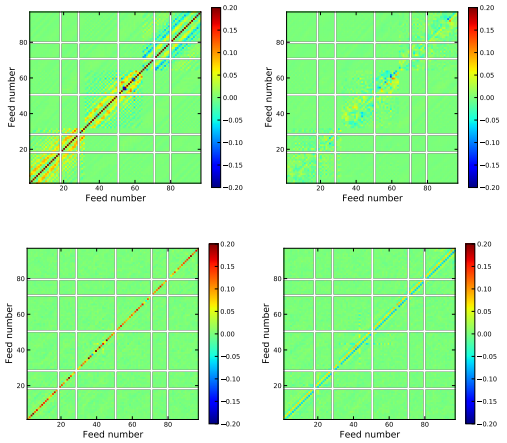

Figure 11. The subtracted nighttime mean visibility matrix (top) and the nighttime mean subtracted visibility matrix (bottom) at observing frequency 750 MHz. Left is for real part, right is for imaginary part. The empty horizontal and vertical lines are masked visibilities due to malfunctioning feeds. The value of the calibrated visibilities have unit brightness temperature K. We have shown the XX polarization visibilities only, the YY polarization visibilities are similar.

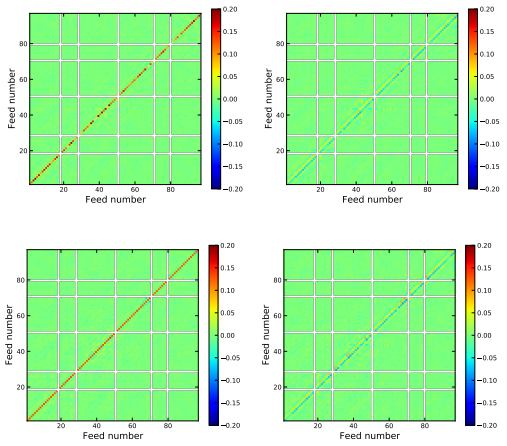

Figure 12. The coupling corrected visibility matrix without diagonal correction (top) and with diagonal correlation (bottom) at observing frequency 750 MHz. Left is for real part, right is for imaginary part. The empty horizontal and vertical lines in the bottom are masked visibilities due to malfunctioning feeds. The value of the calibrated visibilities have unit brightness temperature K. We have shown the XX polarization visibilities only, the YY polarization visibilities are similar.

matrices when there are remaining RFIs or other outliers. These values will be flagged in successive processing steps.

4.3 Map-making

To evaluate the effects of our coupling modeling and correction method applied to Tianlai cylinder array's observational data, we have made maps from one day of visibilities without nighttime mean subtraction and coupling correction, with nighttime mean subtraction and coupling correction, and their difference, as shown in the top, middle, and bottom panels of Figure 14, respectively. The maps are made using the m-mode analysis method (Shaw et al. 2014, 2015;

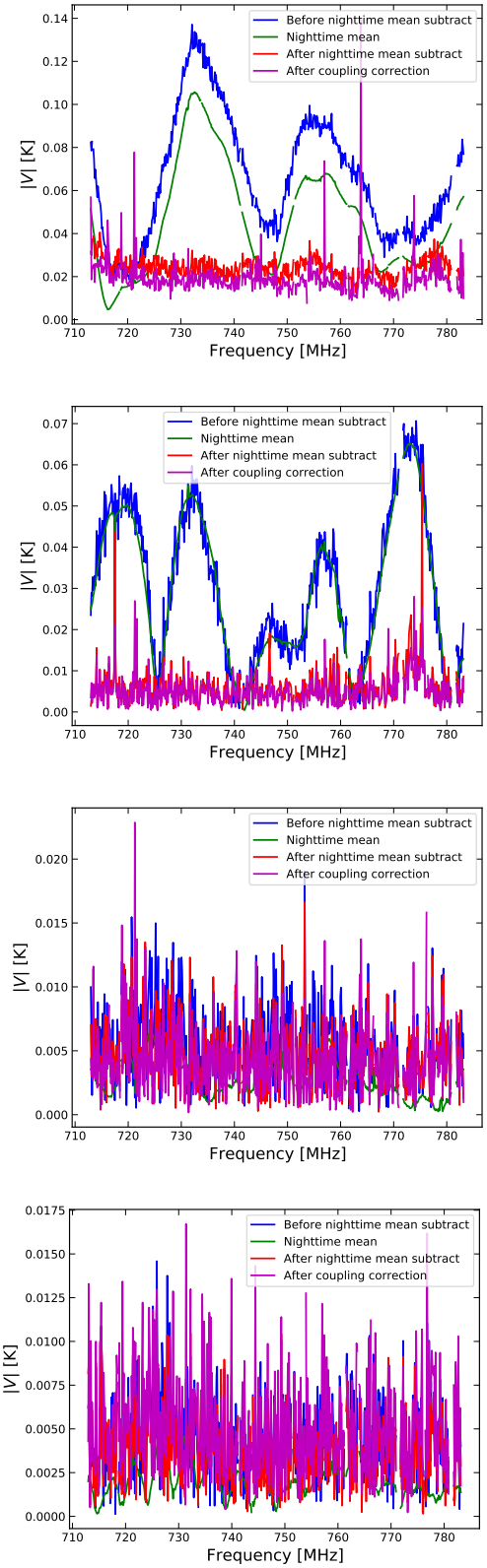

Figure 13. The strong point sources subtracted visibilities (only magnitude) before and after nighttime mean subtraction and coupling correction for four baselines: (10, 11), (10, 20), (10, 40), and (10, 80) at the transit time of the calibrator Cygnus A. We have shown the XX polarization visibilities only, the YY polarization visibilities are similar.

Zhang et al. 2016b,a), taking advantage of the periodicity of the observation due to Earth's rotation. We observe significant artifacts induced by the couplings and DC components in the visibilities. The light and dark stripes near the right boundary are primarily caused by the DC components.

We have masked half an hour of observational data centered at the Sun's transit time, as the Sun's signal is much stronger (approximately two orders of magnitude higher) than other sky objects. Masking its signal before map-making can help avoid its severe negative effects on the map-making results. If DC components are present in the visibility data, the mean of the visibility data will deviate significantly from zero, causing the masked time period, which can be equivalently considered as constant zero observations, to become a gap with sudden changes at the two mask ends. The effects of this gap and the sudden changes at the ends are visible as light and dark stripes on the map (top panel of Figure 14). After subtracting the nighttime mean and performing the coupling correction, the mean of the visibility data becomes closer to zero, resulting in much lower change levels at the two ends of the Sun-masked gap, and the light and dark stripes disappear on the map (middle panel of Figure 14). The two arc-like artifacts, located almost symmetrically on both sides of the masked gap due to the Sun's transit, are contaminations from the Sun entering through the side-lobes of the array beam. Other artifacts, except for the light and dark stripes present on the difference map (bottom panel of Figure 14), are mainly induced by the couplings. Our coupling modeling and correction method can indeed eliminate or alleviate the effects of the couplings present in the observational data and significantly improve the final map-making results.

The maps presented in Figure 14 serve as a demonstration of our coupling modeling and correction method, and are not intended to represent our best map-making results. There are various ways to improve the maps, such as using more days of observational data or restricting the analysis to nighttime data in order to avoid contamination from the Sun. However, these improvements are beyond the scope of this paper and will not be discussed here.

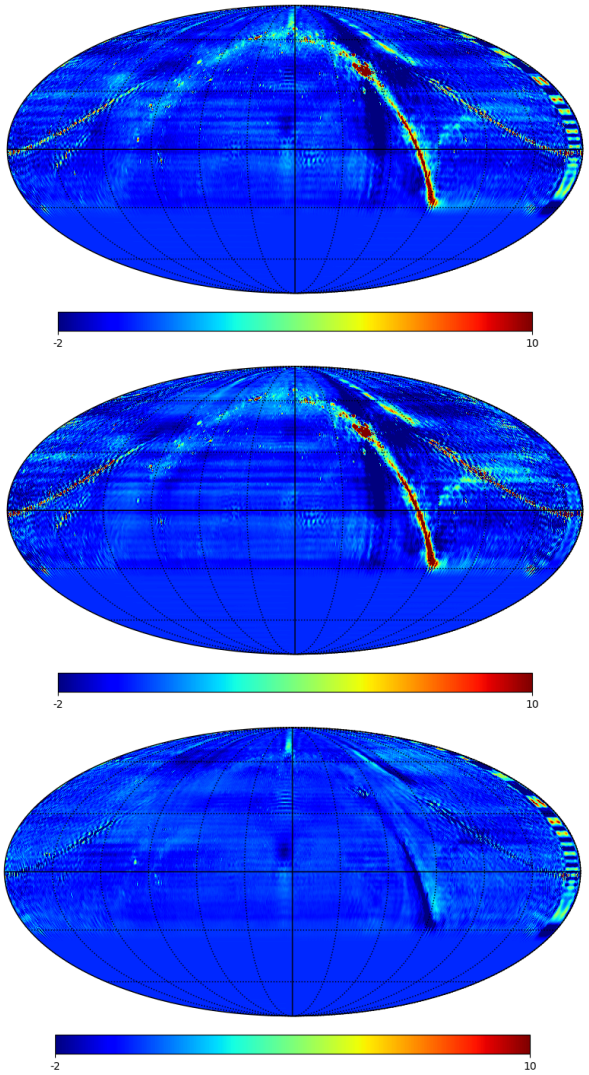

Figure 14. Map made from visibilities without nighttime mean subtraction and coupling correction (top) and with nighttime mean subtraction and coupling correction (middle) and the difference between top and middle.

5 CONCLUSION

We have presented a novel matrix-form mathematical modeling and analysis method for addressing the challenges posed by signal chain reflections and cross coupling between feeds in radio interferometer arrays used for 21 cm cosmological surveys. Our approach unifies the treatment of these systematics, which we collectively refer to as couplings, and provides a robust framework to understand and mitigate their effects on the measurements of the 21 cm signal from Cosmic Dawn, the Epoch of Reionization (EoR), and the post-EoR period.

We outlined a procedure to solve for the coupling matrix and demonstrated how to apply the solved coupling matrix to correct for the effects of couplings in radio interferometry data. Our method was successfully applied to observational data from the Tianlai cylinder array, showcasing its practical utility and effectiveness in real-world scenarios.

The results of this study have important implications for the design and analysis of future 21 cm cosmological surveys. By addressing the issues of signal chain reflections and cross coupling between feeds, our method can significantly improve the quality of the data and the accuracy of the cosmological parameters to be derived. This, in turn, will enable more precise and reliable characterizations of the 21 cm signal and its evolution throughout different cosmic epochs.

The method, though only demonstrated with effectiveness with the observational data observed by the Tianlai cylinder array, is general enough that it can be applied to other radio interferometer arrays, like CHIME, HERA, OVRO-LWA and SKA. Our method could also be combined with other state-of-the-art calibration and foreground subtraction techniques to deliver an even more comprehensive and powerful data processing pipeline for 21 cm cosmological surveys.

In summary, the matrix-form mathematical modeling and removal method for signal chain reflections and cross coupling between feeds presented in this paper constitutes a significant advancement in the field of radio interferometry and promises to greatly enhance our ability to probe the 21 cm signal from Cosmic Dawn, the EoR, and beyond. We anticipate that our approach will play a key role in addressing the challenges associated with radio interferometry and will contribute to our understanding of the early Universe's history and its evolution.

ACKNOWLEDGEMENTS

We thank XXX and XXX for discussions. We acknowledge the support by National SKA Program of China, No.2022SKA0110100.

Software: tlpipe (Zuo et al. 2021), h5py (Collette et al. 2021), healpy (Zonca et al. 2019), Matplotlib (Hunter 2007), NumPy (Harris et al. 2020), SciPy (Virtanen et al. 2020)

APPENDIX A: THE IMPACT OF COUPLING ON THE EIGENVECTOR-BASED CALIBRATION METHOD

In our previous work (Zuo et al. 2019), we presented an eigenvector-based formalism to calibrate radio interferometer arrays and applied it to the cylinder pathfinder of the Tianlai experiment. However, we did not consider the impact of coupling on the calibration method in that work. Here, we demonstrate that the coupling has only a minor effect on the eigenvector-based calibration method, and combining it with the coupling modeling and correction method discussed in this paper can accurately calibrate the array and mitigate the coupling effects.

We begin with the measurement equation of the visibility observed by a two-element interferometer, given by

$$V_{ij} = g_i g_j^* \int A_i(\hat{\boldsymbol{n}}) A_j^*(\hat{\boldsymbol{n}}) I(\hat{\boldsymbol{n}}) e^{2\pi i \hat{\boldsymbol{n}}\cdot\boldsymbol{u}_{ij}}\, d^2\hat{\boldsymbol{n}} + n_{ij}, \tag{A1}$$

where $\boldsymbol{u}_{ij} = (\boldsymbol{r}_i - \boldsymbol{r}_j)/\lambda$ is the baseline vector between the two feeds in units of wavelength, and $I(\hat{\boldsymbol{n}})$ is the sky intensity distribution.

When there is a strong radio point source with flux S_c at direction $\hat{\boldsymbol{n}}_0$ that dominates,

$$\begin{aligned} V_{ij} &= \left(g_i S_c^{\frac{1}{2}} A_i(\hat{\boldsymbol{n}}_0) e^{2\pi i \hat{\boldsymbol{n}}_0\cdot\boldsymbol{u}_i}\right)\left(g_j S_c^{\frac{1}{2}} A_j(\hat{\boldsymbol{n}}_0) e^{2\pi i \hat{\boldsymbol{n}}_0\cdot\boldsymbol{u}_j}\right)^* + r_{ij} \\ &= (g_i s_i)(g_j s_j)^* + r_{ij} \end{aligned} \tag{A2}$$

holds, where $s_i = S_c^{\frac{1}{2}} A_i(\hat{\boldsymbol{n}}_0) e^{2\pi i \hat{\boldsymbol{n}}_0\cdot\boldsymbol{u}_i}$ is the voltage signal of feed i induced by the point source alone, and r_{ij} are the sum of visibility of all other objects on the sky except the strong point source and the noise. Write it in vector-matrix form, this is

$$\boldsymbol{V}' = \boldsymbol{V}'_0 + \boldsymbol{R}' = \boldsymbol{G}\boldsymbol{s}\boldsymbol{s}^\dagger\boldsymbol{G}^\dagger + \boldsymbol{R}' = (\boldsymbol{g}\odot\boldsymbol{s})(\boldsymbol{g}\odot\boldsymbol{s})^\dagger + \boldsymbol{R}', \tag{A3}$$

where the gain matrix $\boldsymbol{G}$ is a diagonal matrix, and $\boldsymbol{g}$ is a vector formed from the diagonals of $\boldsymbol{G}$, and $\odot$ is element-wise product. Here the prime indicates that the elements of the matrices are un-calibrated visibilities.

From $\boldsymbol{V}'_0 = (\boldsymbol{g}\odot\boldsymbol{s})(\boldsymbol{g}\odot\boldsymbol{s})^\dagger$, we see $\boldsymbol{V}'_0$ is a rank-1 Hermitian matrix, so it has only one non-zero eigenvalue. With its eigen-decomposition $\boldsymbol{V}'_0 = \lambda\boldsymbol{x}\boldsymbol{x}^\dagger = \boldsymbol{s}'\boldsymbol{s}'^\dagger$, where $\boldsymbol{s}' = \lambda^{\frac{1}{2}}\boldsymbol{x}$ is an (un-normalized) eigenvector of $\boldsymbol{V}'_0$ corresponding to its only one non-zero eigenvalue λ, we have $\boldsymbol{g}\odot\boldsymbol{s} = \boldsymbol{s}'$, which gives $\boldsymbol{g} = \boldsymbol{s}'\oslash\boldsymbol{s}$, where $\oslash$ is element-wise division. This is the basic idea of eigenvector-based calibration method. The rank-1 dominant matrix $\boldsymbol{V}'_0$ could be solved by using the stable principal component analysis (SPCA) algorithm given in Zuo et al. (2019).

When taking into account the coupling effects discussed in this paper, we would have

$$\boldsymbol{V}'_0 = (\boldsymbol{I}+\boldsymbol{\Xi})\boldsymbol{G}\boldsymbol{s}\boldsymbol{s}^\dagger\boldsymbol{G}^\dagger(\boldsymbol{I}+\boldsymbol{\Xi}^\dagger) = (\boldsymbol{I}+\boldsymbol{\Xi})(\boldsymbol{g}\odot\boldsymbol{s})(\boldsymbol{g}\odot\boldsymbol{s})^\dagger(\boldsymbol{I}+\boldsymbol{\Xi}^\dagger). \tag{A4}$$

This time, when we still solve for a dominant rank-1 matrix $\boldsymbol{V}'_0 = \boldsymbol{s}'\boldsymbol{s}'^\dagger$ from the un-calibrated and coupling corrupted visibility matrix $\boldsymbol{V}'$, we would have $(\boldsymbol{I}+\boldsymbol{\Xi})(\boldsymbol{g}\odot\boldsymbol{s}) = \boldsymbol{s}'$, the solution $\boldsymbol{g}' = \boldsymbol{s}'\oslash\boldsymbol{s} \neq \boldsymbol{g}$, i.e. the gain $\boldsymbol{g}'$ solved by the eigenvector-based calibration method does not equal to the true gain $\boldsymbol{g}$. However, we find that $\boldsymbol{g}'$ is close to $\boldsymbol{g}$, the coupling has only a minor impact on the eigenvector-based calibration method.

We define $\boldsymbol{d} = \boldsymbol{g}'\oslash\boldsymbol{g}$ and diagonal matrix $\boldsymbol{G}'$ and $\boldsymbol{D}$ whose diagonal elements form the vector $\boldsymbol{g}'$ and $\boldsymbol{d}$ respectively, then there is $\boldsymbol{G} = \boldsymbol{D}^{-1}\boldsymbol{G}'$. Substitute this expression into Equation 7, we would have

$$\boldsymbol{V}' = (\boldsymbol{I}+\boldsymbol{\Xi})\boldsymbol{D}^{-1}\boldsymbol{G}'\boldsymbol{V}\boldsymbol{G}'^\dagger\boldsymbol{D}^{-\dagger}(\boldsymbol{I}+\boldsymbol{\Xi}^\dagger). \tag{A5}$$

Now as long as we take $(\boldsymbol{I}+\boldsymbol{\Xi})\boldsymbol{D}^{-1}$ as $(\boldsymbol{I}+\boldsymbol{\Xi})$, the combination of the eigenvector-based calibration method and the coupling modeling and correction method discussed in this paper would accurately calibrate the array and mitigate the effects of the coupling.

REFERENCES

Amiri M., et al., 2023, ApJ, 947, 16

Ansari R., Le Goff J. ., Magneville C., Moniez M., Palanque-Delabrouille N., Rich J., Ruhlmann-Kleider V., Yèche C., 2008, preprint, (arXiv:0807.3614)

Ansari R., et al., 2012, A&A, 540, A129

Bowman J. D., et al., 2013, Publ. Astron. Soc. Australia, 30, e031

Chang T.-C., Pen U.-L., Bandura K., Peterson J. B., 2010, Nature, 466, 463

Chen X., 2012, International Journal of Modern Physics Conference Series, 12, 256

Collette A., et al., 2021, h5py/h5py: 3.5.0, doi:10.5281/zenodo.5585380, https://doi.org/10.5281/zenodo.5585380

Crichton D., et al., 2022, Journal of Astronomical Telescopes, Instruments, and Systems, 8, 011019

Das S., et al., 2018, in Zmuidzinas J., Gao J.-R., eds, Society of Photo-Optical Instrumentation Engineers (SPIE) Conference Series Vol. 10708, Millimeter, Submillimeter, and Far-Infrared Detectors and Instrumentation for Astronomy IX. p. 1070836 (arXiv:1806.04698), doi:10.1117/12.2313031

DeBoer D. R., et al., 2017, PASP, 129, 045001

Eastwood M. W., et al., 2018, AJ, 156, 32

Eastwood M. W., et al., 2019, AJ, 158, 84

Furlanetto S. R., Oh S. P., Briggs F. H., 2006, Phys. Rep., 433, 181

Gehlot B. K., et al., 2019, MNRAS, 488, 4271

Hamaker J. P., Bregman J. D., Sault R. J., 1996, A&AS, 117, 137

Harris C. R., et al., 2020, Nature, 585, 357

Hunter J. D., 2007, Computing in Science Engineering, 9, 90

Intema H. T., Jagannathan P., Mooley K. P., Frail D. A., 2017, A&A, 598, A78

Kern N. S., Parsons A. R., Dillon J. S., Lanman A. E., Fagnoni N., de Lera Acedo E., 2019, The Astrophysical Journal, 884, 105

Kern N. S., et al., 2020, ApJ, 888, 70

Koopmans L., et al., 2015, in Advancing Astrophysics with the Square Kilometre Array (AASKA14). p. 1 (arXiv:1505.07568)

Li J., et al., 2020, Sci. China Phys. Mech. Astron., 63, 129862

Li J.-X., et al., 2021, Research in Astronomy and Astrophysics, 21, 059

Maartens R., Abdalla F. B., Jarvis M., Santos M. G., 2015, arXiv e-prints, p. arXiv:1501.04076

Masui K. W., et al., 2013, ApJ, 763, L20

Morales M. F., Wyithe J. S. B., 2010, ARA&A, 48, 127

Newburgh L. B., et al., 2014, Calibrating CHIME: a new radio interferometer to probe dark energy. p. 91454V, doi:10.1117/12.2056962

Offringa A. R., de Bruyn A. G., Biehl M., Zaroubi S., Bernardi G., Pandey V. N., 2010, MNRAS, 405, 155

Offringa A. R., van de Gronde J. J., Roerdink J. B. T. M., 2012, A&A, 539, A95

Paciga G., et al., 2013, MNRAS, 433, 639

Parsons A. R., et al., 2010, AJ, 139, 1468

Patil A. H., et al., 2017, ApJ, 838, 65

Pritchard J. R., Loeb A., 2012, Reports on Progress in Physics, 75, 086901

Seo H.-J., Dodelson S., Marriner J., Mcginnis D., Stebbins A., Stoughton C., Vallinotto A., 2010, ApJ, 721, 164
Shaw J. R., Sigurdson K., Pen U.-L., Stebbins A., Sitwell M., 2014, ApJ, 781, 57
Shaw J. R., Sigurdson K., Sitwell M., Stebbins A., Pen U.-L., 2015, Phys. Rev. D, 91, 083514
Smirnov O. M., 2011, A&A, 527, A106
Taylor G. B., Carilli C. L., Perley R. A., 1999.
Thompson A. R. A. R., Moran J. M., Swenson George W. (George Warner) ., 1986, Interferometry and synthesis in radio astronomy. New York : Wiley
Vanderlinde K., et al., 2019, in Canadian Long Range Plan for Astronomy and Astrophysics White Papers. p. 28 (arXiv:1911.01777), doi:10.5281/zenodo.3765414
Virtanen P., et al., 2020, Nature Methods, 17, 261
Wu F., et al., 2021, MNRAS, 506, 3455
Xu Y., Wang X., Chen X., 2015, Astrophys. J., 798, 40
Zaroubi S., 2013, in Wiklind T., Mobasher B., Bromm V., eds, Astrophysics and Space Science Library Vol. 396, The First Galaxies. p. 45 (arXiv:1206.0267), doi:10.1007/978-3-642-32362-1_2
Zhang J., Zuo S., Ansari R., Chen X., Li Y., Wu F., Campagne J.-E., Magneville C., 2016a, Res. Astron. Astrophys., 16, 158
Zhang J., Ansari R., Chen X., Campagne J.-E., Magneville C., Wu F., 2016b, Mon. Not. Roy. Astron. Soc., 461, 1950
Zheng H., et al., 2017, MNRAS, 464, 3486
Zonca A., Singer L. P., Lenz D., Reinecke M., Rosset C., Hivon E., Gorski K. M., 2019, Journal of Open Source Software, 4, 1298
Zuo S., Pen U.-L., Wu F., Li J., Stebbins A., Wang Y., Chen X., 2019, AJ, 157, 34
Zuo S., et al., 2021, Astronomy and Computing, 34, 100439
de Oliveira-Costa A., Tegmark M., Gaensler B. M., Jonas J., Landecker T. L., Reich P., 2008, MNRAS, 388, 247

This paper has been typeset from a TEX/LATEX file prepared by the author.